PAPER

Check for updates

Boosting the electrochemical performance with functionalized dry electrodes for practical all-solid-state batteries†

Dongsoo Lee and Arumugam Manthiram [ID] *

All-solid-state batteries (ASSBs) have garnered significant attention due to their superior safety and energy density in comparison to conventional Li-ion batteries (LIBs) that utilize liquid electrolytes. For the practical implementation of ASSBs, the fabrication of sheet-type electrodes is highly desirable. Nevertheless, the development of such sheet-type electrodes poses significant challenges due to the limited chemical stability of sulfide solid electrolytes (SEs) when exposed to commonly used solvents for the slurry-based wet coating electrode. Dry electrodes with polytetrafluoroethylene (PTFE) as a binder are widely employed in ASSBs, but they suffer from limitations in Li$^+$ conductivity due to the insulating nature of PTFE. Here, we introduce a functionalized dry electrode (FDE) incorporating solvate-ionic-liquid infiltrated ethyl cellulose as a binder. The FDE prepared with the LiNi$_{0.8}$Mn$_{0.1}$Co$_{0.1}$O$_2$ cathode demonstrates a high reversible capacity of 181 mA h g^{-1} and outstanding electrochemical performance at room temperature in ASSBs. Even with a high areal capacity of 10 mA h cm^{-2}, a stable cycle performance is achieved with the FDE over 150 cycles. This study presents a novel and practical approach for the development of solvent-free dry electrodes for use in ASSBs.

Introduction

With the rapidly expanding electric vehicle (EV) market, there is an urgent need for the development of all-solid-state Li batteries (ASSBs) due to their inherent advantages of superior safety and high energy density in contrast to conventional Li-ion batteries (LIBs).[1] The incorporation of inorganic solid electrolytes (SEs) as an indispensable component enables the utilization of Li metal anodes and high energy density cathodes, thereby augmenting energy density.[2] Leading-edge sulfide SE materials, such as Li$_{9.54}$Si$_{1.74}$P$_{1.44}$S$_{11.7}$Cl$_{0.3}$ and Li$_{6.6}$Si$_{0.6}$Sb$_{0.5}$S$_5$I, have achieved exceptionally high Li$^+$ conductivity over 10 mS cm^{-1} at room temperature, and ASSBs employing these materials have demonstrated outstanding electrochemical performances comparable with their liquid counterparts.[3,4] Furthermore, the sulfide SEs have a significantly low Young's modulus, which enables facile densification at room temperature.[5]

From a commercialization perspective concerning sulfide SEs, there is a preference for the fabrication of sheet-type electrodes.[6–8] Sheet-type electrodes can facilitate scalable production of ASSBs through roll-to-roll or lamination and stacking processes.[9] Additionally, the utilization of a polymeric binder in conjunction with sheet-type electrodes can effectively

mitigate the stress and strain resulting from the chemo-mechanical degradation incurred during repetitive charging and discharging cycles.[10,11] However, it is worth noting that the development of sheet-type electrodes presents significant challenges due to the limited chemical stability of sulfide SEs in ASSBs.[12,13] This issue arises from the inherent chemical reactivity of sulfide SEs, which renders them incompatible with polar solvents.[14] Even nonpolar solvents, such as toluene, have been found to negatively impact the Li$^+$ conductivity of sulfide SEs.[15]

There have been successful achievements in the fabrication of sheet-type electrodes through a slurry-based wet coating process. The cathode prepared with acrylonitrile butadiene rubber (NBR) as a binder and *para*-xylene as a nonpolar solvent exhibited stable cycling performance with no significant side reaction.[16] Furthermore, when employing a cathode prepared with a solvate-ionic-liquid (SIL) based polymeric binder and dibromomethane as a solvent, outstanding enhancements in both cycle and rate performances have been achieved.[17] Nevertheless, it is essential to recognize that these solvents are not environmentally benign and exhibit suboptimal solubility and(or) dispersibility with polymeric binders.[18–20] Moreover, the emerging dry electrode technique presents distinct advantages when compared to the slurry-based wet coating electrode, encompassing environmental sustainability, cost-effectiveness, chemical compatibility, and production efficiency.[21] As a consequence, sheet-type electrodes *via* a dry electrode process have demonstrated outstanding electrochemical properties,

Materials Science and Engineering Program, Texas Materials Institute, The University of Texas at Austin, Austin, TX, 78712-1591, USA. E-mail: rmanth@mail.utexas.edu

This journal is © The Royal Society of Chemistry 2024

J. Mater. Chem. A, 2024, 12, 3323–3330 | 3323

eliminating the possibility of side reactions between sulfide SEs and the solvent.[22,23] Nevertheless, it is worth noting that sheet-type electrodes utilizing polytetrafluoroethylene (PTFE) as a binder suffer from limitations in Li^+ conductivity due to the electrically and ionically insulating characteristics of PTFE.

In this study, we report a functionalized dry electrode by a solvent-free dry manufacturing process for ASSBs. PTFE is employed to fabricate freestanding sheet-type electrodes integrating solvate-ionic-liquid (SIL) infiltrated ethyl cellulose (EC) as a functionalized dry binder system. The functionalized dry electrode (FDE) prepared with an $LiNi_{0.8}M_{0.1}C_{0.1}O_2$ (NMC-811) cathode demonstrates markedly enhanced electrochemical performance in terms of cyclability and rate capability. Upon careful examination, we reveal that the NMC-811 cathode prepared with only SIL without EC shows limited electrochemical performance in ASSBs. In contrast, the FDE-incorporating SIL-infiltrated EC exhibits outstanding cycle performance, even at a high areal capacity of 10 mA h cm^{-2} (50 mg of NMC-811 cm^{-2}) in ASSBs. It should be noted that these outstanding electrochemical properties are achieved through the solvent-free dry electrode manufacturing process tailored for ASSBs.

Experimental

Synthesis

Li_6PS_5Cl (LPSX) was synthesized through a mechanochemical reaction. Specifically, a mixture, comprising 1.6958 g of LiCl (99.9%, Sigma-Aldrich), 2.2976 g of Li_2S (99.9%, Sigma-Aldrich) and 2.2230 g of P_2S_5 (99.99%, Sigma-Aldrich), was ball milled in a ZrO_2 milling jar with ZrO_2 balls at 500 rpm for a duration of 20 h. Subsequently, the mixture was calcined at 500 °C for 5 h in an Ar atmosphere. $LiNi_{0.8}Mn_{0.1}Co_{0.1}O_2$ was synthesized with a coprecipitation method, as described in a previous report.[24]

Preparation of dry electrodes

To prepare the freestanding reference cathode, NMC-811, LPSX, vapor grown carbon nanofibers (VGCF, Sigma-Aldrich), and PTFE (Sigma-Aldrich) were mixed with a mortar and pestle in a weight ratio of 70 : 27 : 2 : 1 and then rolled with a stainless steel rod. For the fabrication of the FDE, SIL was prepared by mixing lithium bis(trifluoromethanesulfonyl)imide (LiTFSI, Sigma-Aldrich) and tetraethylene glycol dimethyl ether (G4, Sigma-Aldrich) in a 1 : 1 molar ratio. Then, NMC-811, LPSX, VGCF, PTFE, EC (Sigma-Aldrich), and SIL were mixed with a mortar and pestle in a weight ratio of 70 : 25 : 2 : 0.5 : 0.5 : 2 and rolled with a stainless steel rod.

Material characterization

To investigate the morphologies of the cycled cathodes, scanning electron microscopy (SEM) images were observed with an Apreo 2 SEM system. The crystal structure of the materials was analyzed with powder XRD (Rigaku Miniflex 600), utilizing Cu K_α radiation at room temperature. Raman spectra were collected with an Alpha 300 Witec Micro-Raman spectrometer. To characterize the interphase between the cathodes and solid electrolytes, X-ray photoelectron spectrometry (XPS) was employed with Kratos equipment. The binding energy was calibrated with the reference C 1s peak at 284.8 eV, and CasaXPS software was employed for spectral analysis.

Electrochemical characterization

To assemble ASSBs, the freestanding cathode was placed in custom-made stainless-steel cells (12.7 mm diameter) and subjected to a pressure of 350 MPa. Subsequently, 150 mg of LPSX powder was evenly distributed onto the cathode pellet and pressed at 385 MPa. Then, $Li_{0.5}In$ metal foil was affixed to the LPSX side. The ASSBs were assessed at a voltage range of 4.3–2.5 V (vs. Li/Li$^+$) with an external stack pressure of 20 MPa. The electrochemical performance was evaluated with an Arbin cycler. Electrochemical impedance spectroscopy (EIS) data were observed in a frequency range of 1 MHz to 50 mHz with an amplitude of 50 mV using a potentiostat (BioLogic). The galvanostatic intermittent titration technique (GITT) measurements were carried out with a pulse current at 0.2C rate (0.8 mA cm^{-2}) and resting for 1 h. According to the GITT measurements, the Li^+ diffusion coefficient was calculated using the following equation:

$$D_{Li^+} = \frac{4}{\pi\tau}\left(\frac{m_{NMC}V_{NMC}}{M_{NMC}S}\right)^2\left(\frac{\Delta E_s}{\Delta E_\tau}\right)^2(\tau \ll L^2/D)$$

where D_{Li^+} is the Li^+ diffusion coefficient, S is the specific surface area of NMC-811 (0.55 m^2 g^{-1}),[25] τ is the pulse duration, ΔE_s is the steady-state voltage variation, ΔE_t is the transient voltage variation, m_{NMC} is the mass of NMC-811 (25.3 mg), M_{NMC} is the molecular weight of NMC-811 (97.28 g mol^{-1}), and V_{NMC} is the molar volume of NMC-811 (20.33 cm^3 mol^{-1}).[26] To determine the electronic conductivity, ionic blocking cells (SS|cathode|SS) were assembled. The freestanding cathode was positioned within a PEEK cylinder and subjected to a pressure of 350 MPa. A constant voltage of 500 mV was applied for 120 min. For the measurement of Li^+ conductivity of cathodes, electron blocking cells ($Li_{0.5}In$|LPSX|cathode|LPSX|$Li_{0.5}In$) were constructed. Specifically, the freestanding cathode was placed inside a PEEK cylinder and pressed at 350 MPa with stainless steel rods. Afterward, 100 mg of LPSX powder was evenly spread over both sides of the cathode pellet and pressed at 385 MPa. Then, $Li_{0.5}In$ was attached to both sides and subjected to a pressed of 50 MPa.

Results and discussion

SIL, a salt–solvent complex comprising a Li salt and glyme, boasts distinctive attributes, such as remarkable thermal stability, enhanced Li^+ transport, and high oxidation stability.[27,28] Notably, the exceptional thermal stability and Li^+ conductivity of SIL contributes to improved battery safety and electrochemical performance when incorporated into ASSBs.[29] In this study, LiTFSI as a Li salt and G4 as a solvent were employed to prepare the SIL of Li(G4)TFSI. Additionally, EC was introduced in conjunction with SIL to functionalize the electrodes with high Li^+ conductivity. Cellulose based polymers

3324 | J. Mater. Chem. A, 2024, **12**, 3323–3330

This journal is © The Royal Society of Chemistry 2024

have gained widespread application as binders due to the adhesive and dispersive properties in LIBs.[30,31] In the FDE, SIL plays a role in boosting Li$^+$ conductivity and EC functions as an immobilizer of SIL.

LPSX powder and LPSX sheets with PTFE and SIL-infiltrated EC were prepared to investigate the influence of the binder on the Li$^+$ conductivity of Li$_6$PS$_5$Cl (LPSX). Fig. 1a displays the XRD patterns of LPSX powder and freestanding sheets. All three LPSX samples exhibit the characteristic XRD peaks of lithium argyrodite sulfide solid electrolyte (JCPDS card no. 418490).[32] The LPSX sheets prepared with PTFE and SIL infiltrated EC display additional diffraction peaks corresponding to the (108) and (210) planes, which are indicative of the presence of PTFE known as a representative polymer with a crystalline phase.[33] Apart from those peaks, the XRD patterns of both freestanding LPSX sheets remained the same as that of the LPSX powder, which demonstrates the compatibility of LPSX and SIL infiltrated EC without the formation of impurities. To confirm the Li$^+$ conductivity, electron blocking cells were assembled and their electrochemical impedance spectroscopy (EIS) was measured, as shown in Fig. 1b and c. The pristine LPSX powder

exhibits a high Li$^+$ conductivity of 1.6 mS cm^{-1}, which is comparable to the values in the literature.[34] In contrast, the freestanding LPSX sheet with PTFE has an approximately one order lower Li$^+$ conductivity of 0.46 mS cm^{-1}, which is attributed to the insulating nature of PTFE.[17] In contrast to this, the freestanding LPSX sheet with SIL-infiltrated EC demonstrates an elevated Li$^+$ conductivity of 1.2 mS cm^{-1} due to the presence of SIL infiltrated EC. The above results suggest that SIL-infiltrated EC could function as a Li$^+$ conducting binder, enhancing the electrochemical properties in ASSBs without inducing side reactions.

Fig. 1d and e show the Raman spectra of EC in the presence and absence of SIL. The characteristic peak observed at 741.6 cm^{-1} is attributed to Li(G4)TFSI coordinating ion pairs, without the presence of molecules existing in a free state, such as those found in dilute liquid electrolyte.[35] When SIL was introduced into EC, SIL could effectively permeate EC and a distinct peak at 741.6 cm^{-1} was observed. In addition, the peak located at 1244 cm^{-1} indicates the presence of G4 molecules coordinated with Li$^+$.[36] EC with SIL shows a slightly increased peak at 741.6 cm^{-1}. These results indicate that there
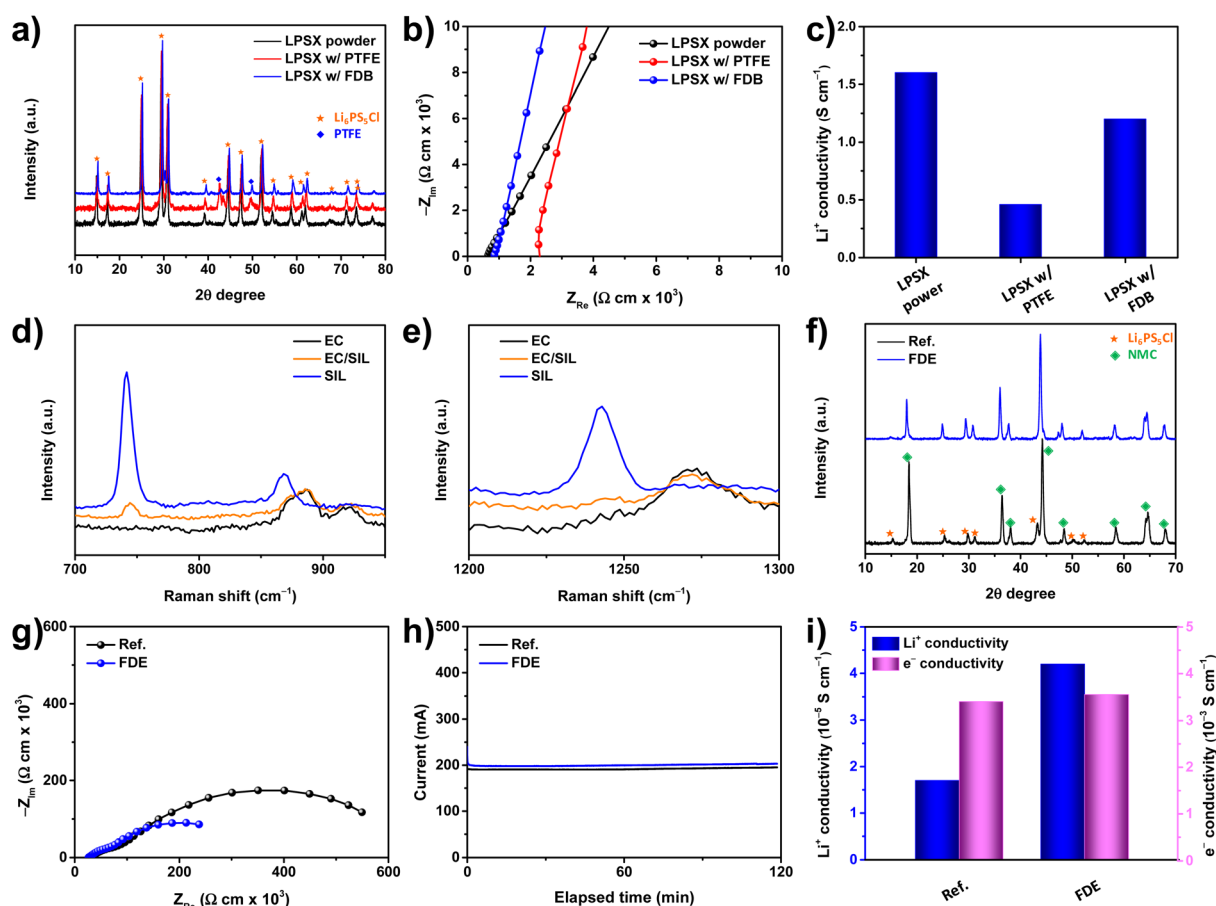

Fig. 1 (a) XRD patterns of LPSX powder and sheets. (b) Nyquist plots measured with electron-blocking cells and (c) their corresponding Li$^+$ conductivity. Raman spectra of EC and SIL in the range of (d) 700 to 950 cm^{-1} and (e) 1200 to 1300 cm^{-1}. (f) XRD patterns of the reference cathode and FDE. (g) Nyquist plots of the electron-blocking cells (Li$_{0.5}$In|LPSX|cathode|LPSX|Li$_{0.5}$In) for the reference cathode and FDE. (h) Current *vs.* elapsed time of the ionic-blocking cells (SS|cathode|SS) for the reference cathode and FDE. (i) Corresponding Li$^+$ and electronic conductivities for the reference cathode and FDE.

This journal is © The Royal Society of Chemistry 2024

J. Mater. Chem. A, 2024, **12**, 3323–3330 | **3325**

is no specific chemical interaction between the components, and SIL is coordinated as an ion pair. In contrast, when SIL is introduced into EC PTFE, it only shows the characteristic peak at 735 cm^{-1}, which is ascribed to the symmetric stretching vibration of CF_2, and the peaks at 1218 and 1244.5 cm^{-1} correspond to the bending vibrations of C–F–C groups involving slight deformations of the bond angles (Fig. S1†).[37,38] SIL has poor wettability in PTFE due to its high hydrophobicity.

The XRD patterns of the cathode reveal the typical NMC-811 peaks with a high intensity peak at 18° corresponding to the (003) reflection of NMC, indicating the α-NaFeO$_2$ structure (Fig. S2†).[24] To investigate the electronic and ionic conductivity of cathodes, freestanding dry electrodes were fabricated with NMC-811 as a cathode active material (Fig. S3†). The reference cathode prepared with PTFE and the FDE show no perceptible difference, showing only NMC and LPSX peaks as shown in Fig. 1f. The result demonstrates that there is no chemical reaction between the components in the FDE. To assess the Li$^+$ conductivity of cathodes, electron-blocking cells (Li$_{0.5}$-In|LPSX|cathode|LPSX|Li$_{0.5}$In) were assembled, and their EIS data were collected (Fig. 1g). The overall semicircles in the EIS represent the Li$^+$ resistance of the composite cathodes. In addition, Li$^+$-blocking cells composed of stainless steel (SS)|cathode|SS were employed to evaluate the electronic conductivity of cathodes through the DC polarization method (Fig. 1h). The calculated Li$^+$ and electronic conductivities of cathodes are presented in Fig. 1i. The reference cathode and the FDE show similar electronic conductivities of 3.4×10^{-3} and 3.5×10^{-3} S cm^{-1}, respectively. However, the FDE displays a notably higher Li$^+$ conductivity of 4.2×10^{-5} S cm^{-1} compared to the reference cathode (1.7×10^{-5} S cm^{-1}). The SIL-infiltrated EC could improve the Li$^+$ conductivity of the FDE, which can boost the electrochemical performance of ASSBs.

To evaluate the electrochemical performance, ASSBs consisting of cathode|LPSX|Li$_{0.5}$In were assembled. Fig. 2a shows the discharging rate performances of cathodes, evaluated up to 2C rate. The areal mass loading of NMC-811 was 20 mg cm^{-2} corresponding to the areal capacity of 4 mA h cm^{-2} for both electrodes. All cells were charged at the same current density of 0.4 mA cm^{-2} (0.1C). In the initial cycles, the FDE exhibits a high capacity of 181 mA h g^{-1} with a high coulombic efficiency of 80.1% compared to the reference cathode (149 mA h g^{-1} and 77.7%). The reference cathode exhibits fast capacity fade at 1C rate, but subsequently recovers when the rate is reduced to 0.1C rate. In contrast, the FDE exhibits outstanding rate performance up to 2C rate, showing high capacities of 140 mA h g^{-1} at 1C rate and 88 mA h g^{-1} at 2C rate. The voltage profiles reveal lower polarization in the FDE compared to the reference cathode (Fig. 2b and c). The improved rate capability of the FDE can be attributed to the high Li$^+$ conductivity facilitated by SIL-infiltrated EC. The cycle performances of the cathodes were evaluated at 0.2C rate following the initial formation cycle at 0.05C rate and two additional cycles at 0.1C rate. The FDE exhibits outstanding cycle performance over 300 cycles compared to that of the reference cathode (Fig. 2d). The capacity retention of the FDE is 79.9% and 74.0% after 200 and 300 cycles, respectively. In contrast, the reference cathode displays

gradual capacity degradation with the capacity retentions of 57.8% and 52.1% after 200 and 300 cycles, respectively. The excellent cycle performance could originate from the highly Li$^+$ conductive dry binder system and a uniform current distribution within the FDE. The SEM images after 200 cycles show distinct differences in the morphologies of the reference cathode and FDE compared to their pristine morphologies before cycling (Fig. S4†). The reference cathode exhibits severe microcracks and particle rupture, which is primarily attributed to the inhomogeneous contact and consequent non-uniform current distribution. In contrast, the FDE shows no noticeable microcracks, retaining its original morphology. The formation of microcracks significantly impacts the electrochemical performance by disrupting the Li$^+$ pathway and promoting inhomogeneous current distribution in ASSBs. Furthermore, the FDE with a low SIL content presents enhanced electrochemical properties compared to those of the reference cathode (Fig. S5†). Considering the energy density of the cathode, the preparation of the electrode with higher SIL content was excluded in this study. The unique characteristics of the FDE with high Li$^+$ conductivity could be beneficial to the homogeneous current distribution and fast Li$^+$ transport. This, in turn, contributes to the preservation of particle integrity, preventing the formation of microcracks during cycling.

The EIS of cathodes was observed to examine the interfacial resistances after 50 cycles (Fig. 2e). Both cathodes exhibit similar ohmic resistances (R_s) and cathode–electrolyte interphase resistance (R_{CEI}), as detailed in Table 1. However, there is a significant difference in the charge-transfer resistance (R_{CT}). The FDE exhibits a low R_{CT} of 83.6 Ω, whereas the reference cathode shows a substantially higher R_{CT} of 363.6 Ω. The discharge voltage profile and the corresponding polarization observed by the galvanostatic intermittent titration technique (GITT) are presented in Fig. 2f. A lower polarization for the FDE is observed compared to the reference cathode at a current density of 0.2C rate in the entire region. Based on the GITT results, the Li$^+$-ion diffusivity in the reference cathode and the FDE was calculated, as shown in Fig. 2g. The Li$^+$-ion diffusion coefficients in the FDE are higher than those in the reference cathode in all voltage regions. These results indicate that implementing the FDE system can enhance the electrochemical performance by facilitating the charge-transfer kinetics, which can be attributed to the increased Li$^+$ conductivity and the intimate contact. Furthermore, a distinct semicircle is observed in the cathode symmetric cell prepared with the reference cathode with SIL, which implies the formation of an interfacial resistive layer of LPSX with SIL (Fig. 2h).[39] In contrast to this, the symmetric cell prepared with the FDE only shows the diffusion tail. The NMC-811 cathode prepared with PTFE and SIL initially exhibits improved capacities comparable to those of the FDE (Fig. S6†). However, the cathode prepared with PTFE and SIL shows rapid capacity degradation compared to the FDE. Generally, it is known that SIL is compatible with sulfide SE materials.[17] Therefore, the poor cycle performance of the cathode with PTFE and SIL could be attributed to the limited affinity between PTFE and SIL because SIL can be mobile and not act as a conducting bridge in the cathode composite. These

3326 | *J. Mater. Chem. A*, 2024, **12**, 3323–3330
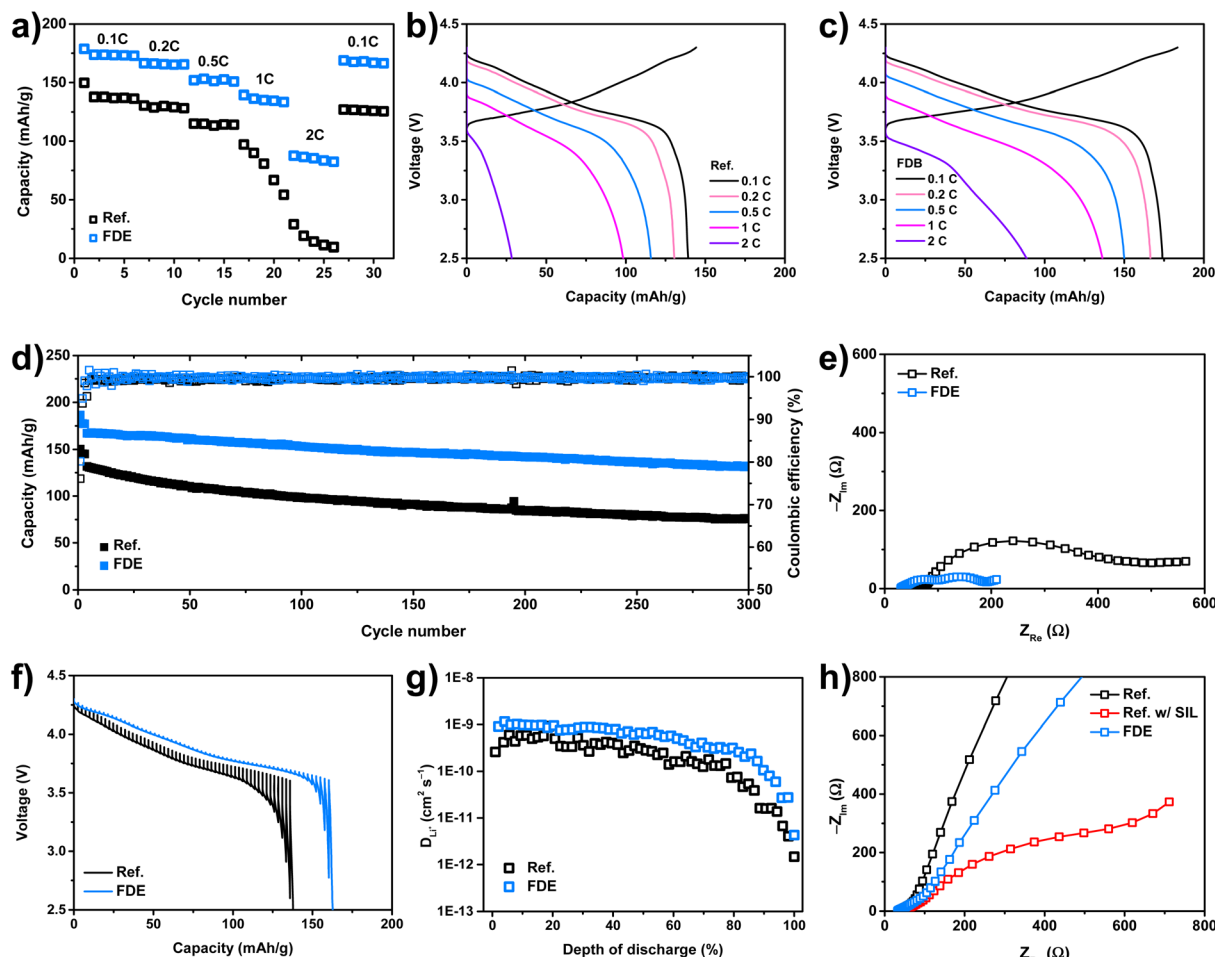
This journal is © The Royal Society of Chemistry 2024

Fig. 2 (a) Rate capability of the reference cathode and FDE up to 2C rate. Voltage profiles at various rates for (b) the reference cathode and (c) FDE. (d) Cycle performance at 0.2C rate at room temperature. (e) Nyquist plots after 50 cycles. (f) Voltage profiles obtained from GITT at 0.2C rate and (g) corresponding Li$^+$-ion diffusion coefficients of the reference cathode and FDE. (h) Nyquist plots of the symmetric cathode cells. All cathodes were prepared with an areal capacity of 4 mA h cm^{-2} (20 mg of NMC-811 cm^{-2}).

Table 1 Resistance parameters of the reference cathode and FDE after 50 cycles

	R_s	R_{CEI}	R_{CT}
Ref.	34.2	49.2	363.6
FDE	30.4	52.2	83.6

findings suggest that EC can function as an immobilizer of SIL, thereby serving as an effective conducting bridge in the cathode in ASSBs.

The *in situ* EIS at the initial cycle was measured to understand the interfacial resistance (Fig. 3a–c). The reference cathode and FDE present a similar trend during the initial cycle, with an increase in the overall resistance up to the fully charged state of 4.3 V (*vs.* Li/Li$^+$). However, the FDE exhibits significantly lower resistances during charging and discharging compared to those of the reference cathode. The improved charge-transfer kinetics attributed to the FDE can lead to the enhanced electrochemical performance characterized by a low interfacial

resistance. To investigate the interfacial degradation of the cathodes, XPS measurements were conducted. Fig. 3d and e display the S 2p spectrum of the reference cathode and FDE after 50 cycles. In both cathodes, the main doublet appears at 161.5 eV, corresponding to LPSX.[3] The additional doublet peaks observed at 162.8 eV and 163.5 eV correspond to the oxidized sulfur species resulting from the decomposition of LPSX.[40] Furthermore, the double peaks at 167.1 eV and 169.6 eV indicate the presence of sulfite and sulfate, which are associated with the side reactions between NMC-811 and LPSX due to their chemical incompatibility.[41] Fig. 3f and g present the P 2p spectrum of the reference cathode and FDE after 50 cycles. The double peaks at 132.9 and 133.8 eV indicate the presence of P$_2$S$_x$ species.[42] In addition, doublet peaks at 133.9 and 134.7 eV were observed, which can be assigned to phosphates resulting from the incompatibility of the layered oxide cathode and LPSX. Overall, the reference cathode and FDE exhibit typical interphase layers related to the layered oxide cathode and sulfide SE after cycling. Nevertheless, the FDE exhibits a less pronounced formation of the resistive layers, a feature that can positively influence the improved electrochemical properties.
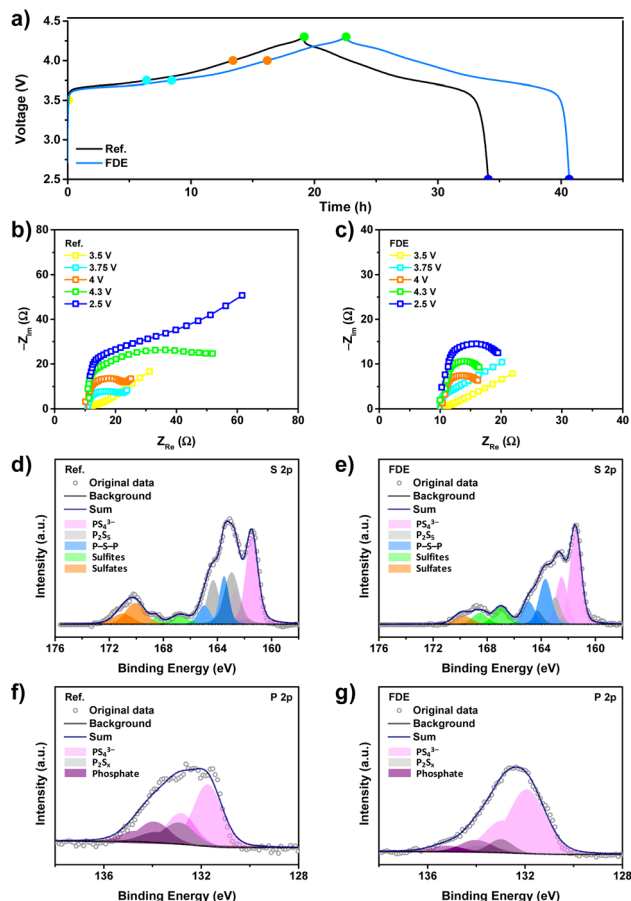
Fig. 3 (a) Initial voltage profiles of the reference cathode and FDE. Nyquist plots of (b) the reference cathode and (c) FDE at the first cycle. XPS spectra of the S 2p core-level regions of (d) the reference cathode and (e) FDE after 50 cycles. XPS spectra of the P 2p core-level regions of (f) the reference cathode and (g) FDE after 50 cycles.

Fig. 4 (a) Initial voltage profiles and (b) cycle performance of the reference cathode and FDE at 0.1C at room temperature. All cathodes were prepared with an areal capacity of 10 mA h cm^{-2} (50 mg of NMC-811 cm^{-2}).

To demonstrate the practical use of the FDE, the electrodes were prepared with a high areal capacity of 10 mA h cm^{-2} (50 mg of NMC-811 cm^{-2}) and evaluated at 0.1C rate. With the increase in areal capacity, the reference cathode exhibits a low initial discharging capacity of 119 mA h g^{-1} with a coulombic efficiency of 78.2% due to the elevated overpotentials caused by the longer Li$^+$ diffusion pathway, as shown in Fig. 4a. In contrast, the FDE exhibits a notably higher initial discharging capacity of 166 mA h g^{-1} with a higher coulombic efficiency of 80.6%. Furthermore, the FDE shows outstanding cycle performance with a high capacity retention of 80.1% after 150 cycles, as shown in Fig. 4b. On the other hand, the reference cathode shows a gradual capacity degradation, showing a capacity retention of 47.9% after 150 cycles. The particle contacts within the cathode are of paramount importance for achieving optimal electrochemical performance in ASSBs. The conventional cathodes employing insulating binders, such as PTFE, encounter multiple challenges, including contact loss, inhomogeneous current distribution, sluggish Li$^+$ transport, and particle ruptures, resulting in poor electrochemical performances (Fig. 5). In contrast, the FDE incorporating SIL-infiltrated EC
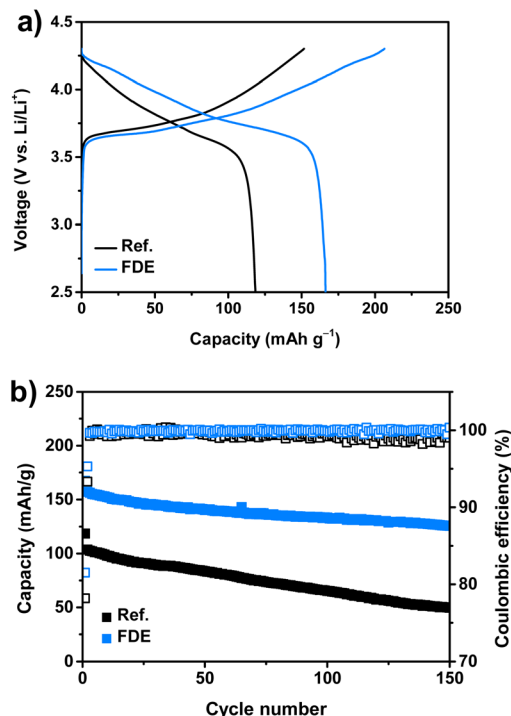
addresses these issues by enhancing the effective contact area through the intimate contact and facilitating Li$^+$ transport, enabling a uniform current distribution. The reversible
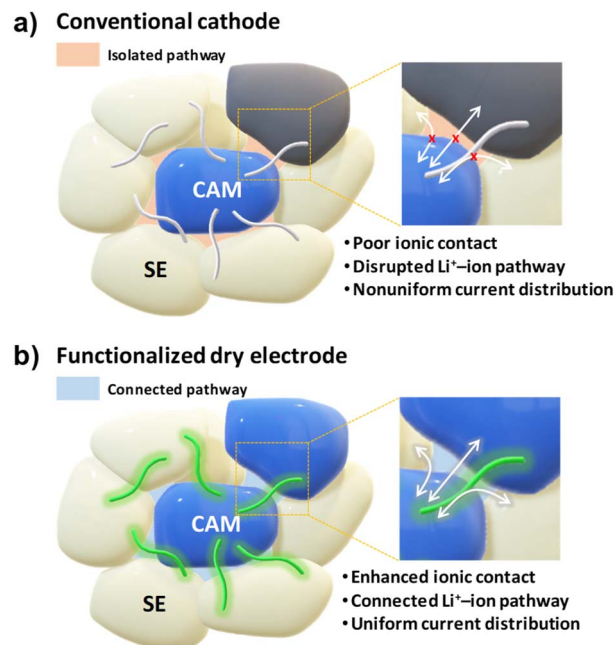

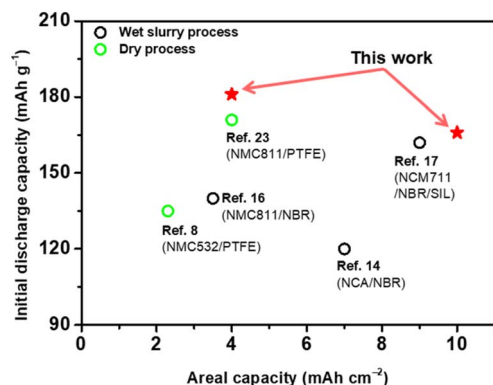Fig. 5 Schematic illustration of (a) the conventional cathode with an ionically insulating binder and (b) FDE.

3328 | J. Mater. Chem. A, 2024, 12, 3323–3330

This journal is © The Royal Society of Chemistry 2024

Fig. 6 Comparison of the initial discharge capacity (mA h g^{-1}) and areal capacity (mA g cm^{-2}) in this work with those of other ASSBs.

discharge capacity (mA h g^{-1}) and areal capacity (mA h cm^{-2}) of the FDE are outstanding compared to those in previous reports (Fig. 6).

Conclusions

In this study, we demonstrated FDEs featuring SIL-infiltrated EC *via* a solvent-free dry process in ASSBs. The freestanding LPSX sheet with SIL-infiltrated EC exhibited excellent Li$^+$ conductivity and demonstrated good chemical compatibility. The unique attributes of the FDE could enable enhanced charge-transfer kinetics as well as increased effective contact area in ASSBs. With these benefits, the FDE exhibited remarkable cycle and rate performance in ASSBs. Furthermore, we demonstrated outstanding cycle performance of the FDE, even under the challenging conditions of an extremely high areal capacity of 10 mA h cm^{-2} over 150 cycles in ASSBs. We believe that this approach can provide valuable insights into the development of solvent-free cathodes for high performance ASSBs.

Conflicts of interest

There are no conflicts to declare.

Acknowledgements

Notes and references

1 S. Randau, D. A. Weber, O. Kötz, R. Koerver, P. Braun, A. Weber, E. Ivers-Tiffée, T. Adermann, J. Kulisch and W. G. Zeier, *Nat. Energy*, 2020, **5**, 259–270.

2 A. Manthiram, X. Yu and S. Wang, *Nat. Rev. Mater.*, 2017, **2**, 1–16.

3 Y. Kato, S. Hori, T. Saito, K. Suzuki, M. Hirayama, A. Mitsui, M. Yonemura, H. Iba and R. Kanno, *Nat. Energy*, 2016, **1**, 1–7.

4 L. Zhou, A. Assoud, Q. Zhang, X. Wu and L. F. Nazar, *J. Am. Chem. Soc.*, 2019, **141**, 19002–19013.

5 R. Koerver, W. Zhang, L. de Biasi, S. Schweidler, A. O. Kondrakov, S. Kolling, T. Brezesinski, P. Hartmann, W. G. Zeier and J. Janek, *Energy Environ. Sci.*, 2018, **11**, 2142–2158.

6 D. H. Kim, D. Y. Oh, K. H. Park, Y. E. Choi, Y. J. Nam, H. A. Lee, S.-M. Lee and Y. S. Jung, *Nano Lett.*, 2017, **17**, 3013–3020.

7 A. Sakuda, K. Kuratani, M. Yamamoto, M. Takahashi, T. Takeuchi and H. Kobayashi, *J. Electrochem. Soc.*, 2017, **164**, A2474.

8 Z. Zhang, L. Wu, D. Zhou, W. Weng and X. Yao, *Nano Lett.*, 2021, **21**, 5233–5239.

9 J. Schnell, T. Günther, T. Knoche, C. Vieider, L. Köhler, A. Just, M. Keller, S. Passerini and G. Reinhart, *J. Power Sources*, 2018, **382**, 160–175.

10 J. Wu, L. Shen, Z. Zhang, G. Liu, Z. Wang, D. Zhou, H. Wan, X. Xu and X. Yao, *Electrochem. Energy Rev.*, 2021, **4**, 101–135.

11 J. Wu, S. Liu, F. Han, X. Yao and C. Wang, *Adv. Mater.*, 2021, **33**, 2000751.

12 Y. Nikodimos, C.-J. Huang, B. W. Taklu, W.-N. Su and B. J. Hwang, *Energy Environ. Sci.*, 2022, **15**, 991–1033.

13 J. Lee, T. Lee, K. Char, K. J. Kim and J. W. Choi, *Acc. Chem. Res.*, 2021, **54**, 3390–3402.

14 S. Ito, S. Fujiki, T. Yamada, Y. Aihara, Y. Park, T. Y. Kim, S.-W. Baek, J.-M. Lee, S. Doo and N. Machida, *J. Power Sources*, 2014, **248**, 943–950.

15 J. Ruhl, L. M. Riegger, M. Ghidiu and W. G. Zeier, *Adv. Energy Sustainability Res.*, 2021, **2**, 2000077.

16 K. Lee, S. Kim, J. Park, S. H. Park, A. Coskun, D. S. Jung, W. Cho and J. W. Choi, *J. Electrochem. Soc.*, 2017, **164**, A2075.

17 D. Y. Oh, Y. J. Nam, K. H. Park, S. H. Jung, K. T. Kim, A. R. Ha and Y. S. Jung, *Adv. Energy Mater.*, 2019, **9**, 1802927.

18 Y. Yang, S. Wu, Y. Zhang, C. Liu, X. Wei, D. Luo and Z. Lin, *Chem. Eng. J.*, 2021, **406**, 126807.

19 A. Kraytsberg and Y. Ein-Eli, *Adv. Energy Mater.*, 2016, **6**, 1600655.

20 D. Lee, H. Lee, T. Song and U. Paik, *Adv. Energy Mater.*, 2022, **12**, 2200948.

21 Y. Lu, C.-Z. Zhao, H. Yuan, J.-K. Hu, J.-Q. Huang and Q. Zhang, *Matter*, 2022, **5**, 876–898.

22 Y. Li, Y. Wu, T. Ma, Z. Wang, Q. Gao, J. Xu, L. Chen, H. Li and F. Wu, *Adv. Energy Mater.*, 2022, **12**, 2201732.

23 D. Lee and A. Manthiram, *Small Methods*, 2023, 2201680.

24 Q. Xie, Z. Cui and A. Manthiram, *Adv. Mater.*, 2021, **33**, 2100804.

25 S. Deng, Q. Sun, M. Li, K. Adair, C. Yu, J. Li, W. Li, J. Fu, X. Li and R. Li, *Energy Storage Mater.*, 2021, **35**, 661–668.

26 J. Zheng, W. Shi, M. Gu, J. Xiao, P. Zuo, C. Wang and J.-G. Zhang, *J. Electrochem. Soc.*, 2013, **160**, A2212.

27 M. Watanabe, M. L. Thomas, S. Zhang, K. Ueno, T. Yasuda and K. Dokko, *Chem. Rev.*, 2017, **117**, 7190–7239.

This journal is © The Royal Society of Chemistry 2024

J. Mater. Chem. A, 2024, **12**, 3323–3330 | **3329**

28 T. Mandai, K. Yoshida, S. Tsuzuki, R. Nozawa, H. Masu, K. Ueno, K. Dokko and M. Watanabe, *J. Phys. Chem. B*, 2015, **119**, 1523–1534.

29 L. Su, E. Jo and A. Manthiram, *ACS Energy Lett.*, 2022, **7**, 2165–2172.

30 J.-H. Lee, U. Paik, V. A. Hackley and Y.-M. Choi, *J. Electrochem. Soc.*, 2005, **152**, A1763.

31 D. Lee, H. Park, A. Goliaszewski, Y.-k. Byeun, T. Song and U. Paik, *Ind. Eng. Chem. Res.*, 2019, **58**, 8123–8130.

32 N. C. Rosero-Navarro, A. Miura and K. Tadanaga, *J. Sol-Gel Sci. Technol.*, 2019, **89**, 303–309.

33 E. N. Brown and D. M. Dattelbaum, *Polymer*, 2005, **46**, 3056–3068.

34 N. Kamaya, K. Homma, Y. Yamakawa, M. Hirayama, R. Kanno, M. Yonemura, T. Kamiyama, Y. Kato, S. Hama and K. Kawamoto, *Nat. Mater.*, 2011, **10**, 682–686.

35 J. Fawdon, J. Ihli, F. L. Mantia and M. Pasta, *Nat. Commun.*, 2021, **12**, 4053.

36 P. Shi, H. Zheng, X. Liang, Y. Sun, S. Cheng, C. Chen and H. Xiang, *Chem. Commun.*, 2018, **54**, 4453–4456.

37 A. Gruger, A. Régis, T. Schmatko and P. Colomban, *Vib. Spectrosc.*, 2001, **26**, 215–225.

38 J. Koenig and F. Boerio, *J. Chem. Phys.*, 1969, **50**, 2823–2829.

39 J. Jang, Y.-T. Chen, G. Deysher, D. Cheng, S.-Y. Ham, A. Cronk, P. Ridley, H. Yang, B. Sayahpour and B. Han, *ACS Energy Lett.*, 2022, **7**, 2531–2539.

40 L. Ye and X. Li, *Nature*, 2021, **593**, 218–222.

41 M. Fantauzzi, B. Elsener, D. Atzei, A. Rigoldi and A. Rossi, *RSC Adv.*, 2015, **5**, 75953–75963.

42 J. Auvergniot, A. Cassel, J.-B. Ledeuil, V. Viallet, V. Seznec and R. Dedryvère, *Chem. Mater.*, 2017, **29**, 3883–3890.

3330 | *J. Mater. Chem. A*, 2024, **12**, 3323–3330

This journal is © The Royal Society of Chemistry 2024